Structural properties in RFe_2O_4 compounds (R = Tm, Yb, and Lu)

J. Blasco,[1,*] S. Lafuerza,[2] J. García,[1] and G. Subías[1]

[1]*Instituto de Ciencia de Materiales de Aragón and Departamento de Física de la Materia Condensada, Consejo Superior de Investigaciones Científicas y Universidad de Zaragoza, 50009 Zaragoza, Spain*

[2]*The European Synchrotron Radiation Facility (ESRF), 71, Avenue des Martyrs, 38042 Grenoble Cedex, France*

(Received 26 June 2014; revised manuscript received 15 September 2014; published 29 September 2014)

We report a complete characterization of the crystal structure between 400 and 80 K for RFe_2O_4 (R = Rm, Yb, and Lu) compounds using high resolution x-ray synchrotron powder diffraction. The three samples have a hexagonal structure (space group $R\bar{3}m$) characterized by a sequence of double layers of mixed valence iron and oxygen atoms forming two-dimensional triangular layers separated by a single R-O layer along the c axis. This structure is stable down to 80 K for $TmFe_2O_4$ and $YbFe_2O_4$ though a sudden expansion in the c axis is observed at around 300 K coupled to a variation in the electrical properties. However, $LuFe_2O_4$ exhibits two structural transitions upon cooling. The splitting of some reflections and the occurrence of superstructure peaks below 320 K reveal a structural phase transition. The unit cell is monoclinic (space group $C2/m$), and there are four nonequivalent Fe sites with a maximum charge disproportionation of 0.5 e. The hexagonal to monoclinic transition is characterized by a sudden expansion of the c axis on cooling, and it seems to be driven by the condensation of Y_2 modes. At lower temperatures ($\sim$170 K) additional splitting of several peaks indicate that the unit cell is no longer monoclinic but triclinic (space group $P\bar{1}$). This transition is characterized by a contraction of the monoclinic ab plane, while the c axis remains almost unchanged. There are six nonequivalent Fe sites in the triclinic cell, and the charge disproportionation magnitude is little affected.

DOI: 10.1103/PhysRevB.90.094119 PACS number(s): 61.05.cp, 61.66.Fn, 64.60.−i, 75.47.Lx

I. INTRODUCTION

Materials exhibiting ferromagnetism and ferroelectricity simultaneously are a special class of multiferroic compounds with promising technological applications [1]. The combination of both properties has proven to be difficult and tends to have a weak coupling because the microscopic mechanisms for ferroelectric and ferromagnetic orderings are very different from each other and normally these two order parameters are reciprocally exclusive [2,3]. Therefore, there is intense research to find new routes to combine both properties, and a striking approach was the prediction of ferroelectricity in systems with charge ordering (CO).

The proposed example of ferroelectricity associated with a CO state is supposed to be $LuFe_2O_4$ [4]. This compound undergoes a CO transition at $T_{CO} \sim 320$ K. Above T_{CO}, $LuFe_2O_4$ is a mixed valence oxide and the hexagonal crystal structure can be viewed as a stack of alternating triangular Lu-O single layer and triangular Fe-O double layers (hereafter denoted as Fe bilayer) along the hexagonal c axis. Crystal symmetry belongs to the rhombohedral system with space group $R\bar{3}m$. Below T_{CO}, CO of an even mixture of Fe^{2+} and Fe^{3+} ions was postulated to render the Fe bilayers polar. The checkerboard distribution of both cations is not favorable due to the triangular iron lattice [5]. Hence, the polar bilayer is stabilized by making one of the layers rich in Fe^{2+} and the other rich in Fe^{3+} [4,6]. This special CO pattern permits a possible ferroelectric ordering between consecutive Fe bilayers and gives an explanation of the pyroelectric effect observed below T_{CO} [4]. Moreover, this compound exhibits a ferrimagnetic ordering [6] at $T_N \sim 240$ K that matches an anomaly in the pyroelectric current measurement, suggesting a significant magnetoelectric effect [7]. Further studies reported a giant magnetodielectric effect at room temperature [8], a large magnetocapacitance effect [9] below T_N, and the magnetization switching by the effect of electric pulses [10], giving additional support for a strong magnetoelectric coupling in this material.

The occurrence of CO and polar Fe bilayers was accepted without direct experimental evidence but recent studies are casting doubt on these assumptions. First, an accurate analysis of the electric properties in $LuFe_2O_4$ has revealed that both giant dielectric permittivity and magnetocapacitance are related to extrinsic effects mainly arising from electrode polarization and conductivity contribution [11–13]. Moreover, detailed polarization measurements failed to find any signature of ferroelectricity in $LuFe_2O_4$ [13,14]. On the other hand, a crystallographic study on a $LuFe_2O_4$ single crystal was successful in refining the crystal structure at 210 K (below T_{CO}) using a monoclinic cell with space group $C2/m$. The resulting CO pattern disagrees with the existence of polar bilayers, and de Groot *et al.* [15] proposed instead an antiferroelectric stacking of charged Fe^{3+}(rich)- and Fe^{2+}(rich)-bilayers along the hexagonal c axis. The magnetic and crystal structures were also studied by single crystal neutron diffraction [16]. Christianson *et al.* [16] indicated that long-range magnetic ordering is developed below $T_N = 240$ K, and a further structural transition was observed at 175 K. The latter was typified as magnetostructural transition and was characterized by the broadening of a number of diffraction peaks and the growth of a diffuse component to the magnetic scattering. Therefore, controversial results have been reported on $LuFe_2O_4$, and a full description of the crystal structure at low temperatures together with the correspondent CO pattern have not yet been elucidated.

Regarding the other two samples, $TmFe_2O_4$ and $YbFe_2O_4$, far fewer papers were devoted to their study. Both samples are isostructural to $LuFe_2O_4$, exhibiting the same rhombohedral

*Corresponding author: jbc@unizar.es

structure [17]. They show similar electrical transition without a clear signature of significant charge localization in comparison to the large effect observed in the magnetite at the Verwey transition [17]. Magnetization curves of $TmFe_2O_4$ and $YbFe_2O_4$ showed magnetic anomalies at $T_N \sim 240$ K [18,19] similar to ones reported for $LuFe_2O_4$. There is no available data about the low temperature crystal structure of $TmFe_2O_4$ so far, whereas pioneering studies reported no structural changes in $YbFe_2O_4$ on cooling [18]. However, recent studies on $YbFe_2O_4$ single crystals have shown the occurrence of an incommensurate charge density wave in this compound after analyzing the scattering data at 150 K [20].

In the present paper, we report a detailed study of the crystal structures for RFe_2O_4 (R = Tm, Yb, and Lu) compounds between 80 and 400 K using high resolution x-ray synchrotron powder diffraction. Their electric and magnetic properties are also investigated to characterize their phase transitions. This survey allowed us to clarify the differences in the type of charge localization among these ferrites depending on the R cation. In addition, we have determined an unexpected crystal structure for $LuFe_2O_4$ at low temperatures ($\sim$80 K). We note that $LuFe_2O_4$ single crystals present a strong twinning, giving rise to three monoclinic domains rotated by 120° [15,21]. Therefore, the problems of multiple scattering, extinction, and twinning effects can be much reduced or have a minimal effect using powder diffraction, as shown in the present paper. To overcome the loss of information due to peak overlapping, we use synchrotron x-ray powder diffraction, which has proven to have a very high angular resolution [22].

II. EXPERIMENTAL SECTION

RFe_2O_4 samples (R = Tm, Yb, and Lu) were prepared by a solid-state chemistry method. Stoichiometric amounts of R_2O_3 and Fe_2O_3 with nominal purities not less than 99.99% were mixed, ground, and heated at 1200 °C in air for 12 h. The powder was reground, pressed into pellets, and sintered in a CO/CO_2 (2/3) atmosphere for another 12 h. The last step was repeated until obtaining a single phase. Normally, only an additional step is enough. X-ray diffraction patterns were collected at room temperature using a Rigaku D/max-B instrument with a copper rotating anode to control the crystal quality of the samples. The chemical composition of the samples was tested by using the wavelength dispersive x-ray fluorescence spectrometry technique (advant'XP+ model manufactured by ARL). The cationic composition agreed with the nominal one for all samples.

Synchrotron x-ray diffraction patterns were measured at the ID31 beamline at the European Synchrotron Radiation Facility (ESRF; Grenoble, France) [22]. The sample was loaded in a borosilicate glass capillary ($\varphi = 0.5$ mm) and kept spinning during data acquisition. A short wavelength, $\lambda = 0.3542$ Å, was selected to reduce absorption. The value of λ was calibrated using standard silicon. The patterns were collected between 80 and 400 K. The standard acquisition time was around 30 min, but a total acquisition time of 3 h/pattern was used to improve the structural characterization at selected temperatures.

Diffraction patterns were analyzed by the Rietveld method using the FullProf program [23]. The analysis was made by refining either fractional coordinates or amplitudes of condensing modes using the symmetry mode analysis [24]. Both procedures yielded equivalent results. In the second case, the input file with the basis modes was obtained from the AMPLIMODES program [25].

Differential scanning calorimetry (DSC) was measured using a DSC Q-20 from TA Instruments with samples sealed in aluminum pans under a nitrogen atmosphere. The scanning rate was 10 K min^{-1}. Magnetic measurements were carried out between 5 and 300 K by using a commercial Quantum Design superconducting quantum interference device (SQUID) magnetometer, and electrical dc resistivity measurements were made on rectangular bars cut from the pellets with a typical size of $2 \times 2 \times 9$ mm^3. The conventional four-probe configuration was used and electrodes were made using silver paint. The software controlling the experimental setup and the data acquisition was developed using LabVIEW. The electrical resistance was measured dynamically by using an Oxford Instruments cryostat in cooling and heating runs at an average speed of 2 K/min. Both measurements were coincident.

III. RESULTS AND DISCUSSION

A. Physical properties

This study begins with a detailed characterization of the macroscopic physical properties of the RFe_2O_4 samples in order to ensure their quality. Figure 1(a) shows the heating runs of DSC measurements for the three compounds. Two clear peaks are noticeable for $LuFe_2O_4$. A peak at 322.3 K is ascribed to the CO transition, in agreement with reports in literature [13,15]. The phase-transition enthalpy, $\Delta H = \int \Delta C_p(T)\, dT$, is 645 ± 29 J mole^{-1}. The total change in the entropy is $\Delta S = 2.0 \pm 0.1$ J mole^{-1} K^{-1}. This value is approximately $0.24R$, R being the gas constant. A small peak at $T_N = 239.1$ K is in accordance with the magnetic transition reported previously [13]. The small peak size together with the upward convex DSC curve below T_N prevents an accurate determination of ΔH and ΔS associated with this transition. The other two samples show more rounded anomalies at T_{CO} = 307.3 and 283.8 K for $YbFe_2O_4$ and $TmFe_2O_4$, respectively. The calculated enthalpies are 491.5 ± 20 and 236 ± 10 J mole^{-1} for $YbFe_2O_4$ and $TmFe_2O_4$, respectively. These values correspondingly yield a ΔS of 1.6 ± 0.1 and 0.83 ± 0.05 J mole^{-1} K^{-1} for Yb- and Tm-based compounds, respectively. The anomaly ascribed to the magnetic transition is so flattened in both compounds that it is very hard to determine the transition temperature with accuracy, but a bump is noticeable in the DSC curves.

The heat capacity measurements have revealed that T_{CO} decreases as the R size increases. In addition, the enthalpy associated to the transition also decreases with increasing R size. Finally, the small values of ΔS in the CO transition may be ascribed to the presence of either structural correlations in the high temperature phase or structural disorder that remains in the low temperature phase as observed in related oxides [26].

Figure 1(b) shows the temperature dependence of dc resistivity for the three samples. The shape of the curves is very similar to a previous report [17]. The electrical properties of all samples show a semiconducting behavior with an increase of the electrical resistivity as the temperature decreases. A slope

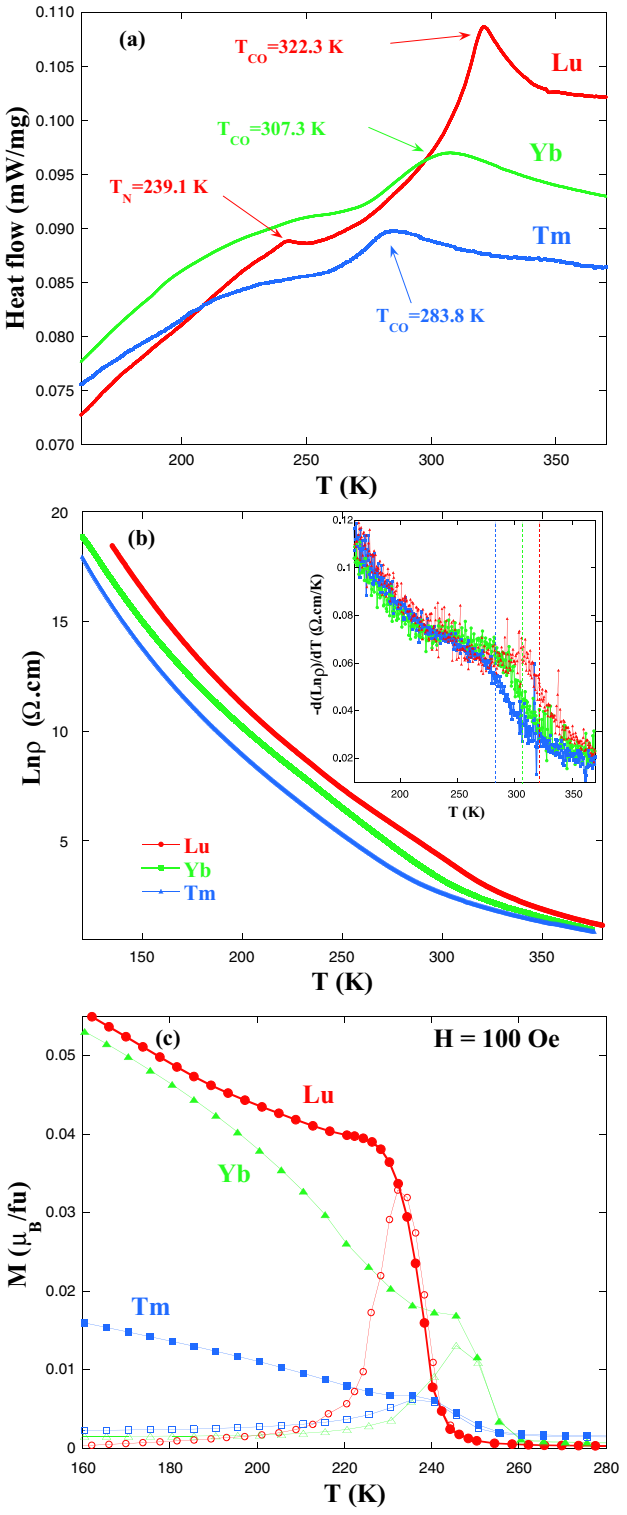

FIG. 1. (Color online) (a) DSC measurements (heating runs) for powder samples of RFe_2O_4 (R = Lu, Yb, and Tm). (b) Electrical resistivity (natural logarithm) vs temperature for the RFe_2O_4 (R = Lu, Yb, and Tm) samples. Inset: Temperature dependence of $-d\ln(\rho)/dT$ (sign changed for the sake of comparison). The vertical lines indicate the temperature of the anomalies detected in DSC curves (T_{CO}). (c) Temperature dependence of magnetization for $LuFe_2O_4$ (circles), $YbFe_2O_4$ (triangles), and $TmFe_2O_4$ (squares). Open and filled symbols correspond to ZFC and FC conditions respectively. The external magnetic field was 100 Oe.

change associated with the CO transition is hardly noticeable in the resistivity curves of Fig. 1(b). The changes are better realized in the derivative curves shown in the inset where a steplike anomaly is clearly seen at T_{CO}, in agreement with the anomalies observed in the DSC curves. The changes in the electrical conductivity are tiny in comparison to the strong localization processes observed in other systems with Verwey-like transitions such as magnetite [27] or YFe_2O_4 [28].

Figure 1(c) shows the temperature dependence of the magnetization in zero-field-cooling (ZFC) and field-cooling (FC) conditions. A strong magnetic irreversibility is observed between both sets of measurements. Zero-field-cooling branches exhibit a peak whereas FC branches show magnetic transitions typical of a ferro- or ferrimagnetic transition. Such behavior is characteristic of materials showing glassy properties and it may be related to competitive magnetic interactions. In the case of $LuFe_2O_4$, the inflection point in the transition observed in FC conditions agrees with the peak ascribed to the magnetic transition in the DSC measurements. In contrast to electrical properties, there is not a clear relationship between R size and magnetic transition temperature. In our case, the highest T_N (inflection point around 252 K) is observed for $YbFe_2O_4$, while $TmFe_2O_4$ has an intermediate value of T_N around 244 K. Overall, the magnetic behavior of our specimens is equivalent to the ones reported in previous studies [18,19,29–31].

B. Crystal structure of $YbFe_2O_4$ and $TmFe_2O_4$

In this section we study the crystal structure of these two compounds because they exhibit very similar structural changes upon cooling. Figure 2 compares the x-ray patterns of $TmFe_2O_4$ collected at 80 and 400 K. Both patterns exhibit the same diffraction peaks, indicating the same crystal structure for this compound in the whole temperature range studied in this paper. Similar results were obtained for $YbFe_2O_4$ (not shown here). Figure 2 also shows the prototype crystal structure of RFe_2O_4 compounds. R atoms are sixfold coordinated with oxygen atoms forming an octahedral environment while the Fe is fivefold coordinated forming trigonal bipyramids sharing edges in the Fe bilayers.

All patterns were refined with the space group $R\bar{3}m$ using the hexagonal setting. Both samples showed a tiny impurity of FeO (<1% in weigh) that was included in the refinements. Table I shows the refined parameters obtained at 400, 300, and 80 K. The high temperature factor observed for all atoms is noticeable, especially for oxygen atoms. This result is likely related to the observation of local distortions by means of x-ray absorption spectroscopy [32], and it may be also related to the incommensurate oxygen displacement patterns outlined for the $YbFe_2O_4$ compound [20].

The unit cell volume of $TmFe_2O_4$ is bigger than that of $YbFe_2O_4$, in agreement with the lanthanide contraction (ionic radii for sixfold-coordinated Yb^{3+} and Tm^{3+} cations are 0.868 and 0.88 Å, respectively [33]). However, the unit cell changes between both samples are not isotropic, and the c axis is higher for $YbFe_2O_4$ while the reverse occurs for the a axis. Temperature dependence of the unit cell is displayed in the Fig. 3. Both samples exhibit a sudden increase of the c axis with decreasing temperature. The onset of this steplike anomaly agrees with the peak observed in DSC curves, so this structural

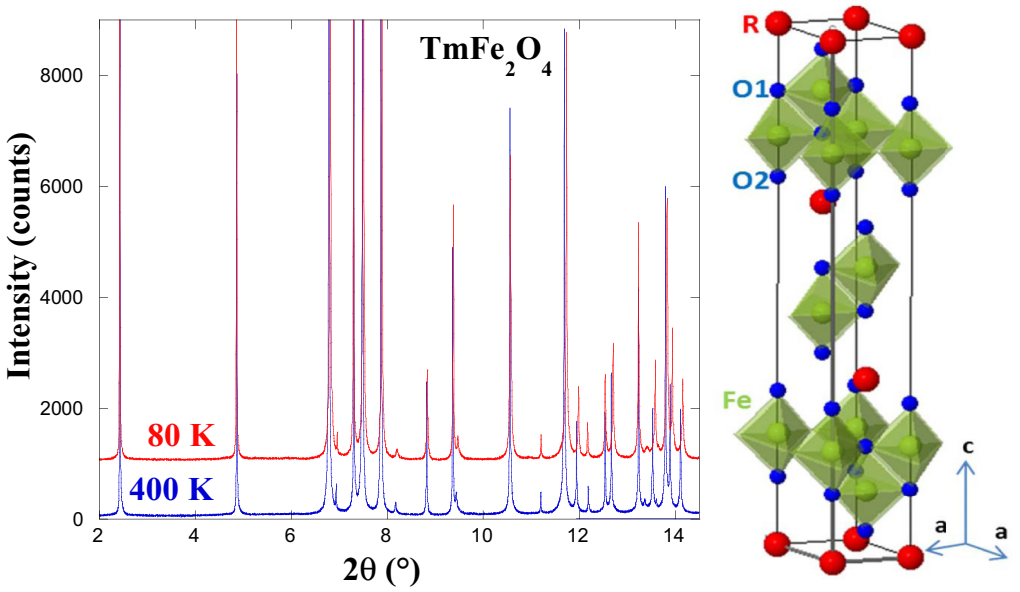

FIG. 2. (Color online) Left: Details of the x-ray patterns for $TmFe_2O_4$ at 80 and 400 K. The former has been shifted upward for the sake of comparison. Right: Hexagonal unit cell volume of RFe_2O_4 compounds.

change seems to be associated to the so-called CO transition. Minor changes are observed in the evolution of the *a* axis, which is not very sensitive to the CO transition except for a turning point in the usual thermal contraction.

More differences can be found between both compounds in the temperature evolution of the refined distances. As indicated in Fig. 2, *R* atoms are coordinated with six oxygen atoms (O2). Fe is coordinated with three oxygen atoms (O1) at the same distance, which are at 120° angles to each other (basal plane) with two more bonds (Fe-O1 and Fe-O2) above and below the basal plane (apical positions). The apical Fe-O1 is significantly longer. The bond valence sums (BVS) method [34,35] was used to determine the valences for each atomic site after structural refinement. Figures 4(a) and 4(b) show the temperature dependence of *R*-O bond lengths and BVS of *R* atoms for $TmFe_2O_4$ and $YbFe_2O_4$, respectively. The Tm-O distance displays a small steplike jump on cooling, which is related to a similar decrease in the BVS value for Tm^{3+}. This valence reaches a value of ∼3.3 at room temperature, which is quite higher than the formal value +3. After cooling, the value slightly decreases down to 3.26, indicating a small relaxation of the steric strain around this atom. In the case of

TABLE I. Refined structural parameters (lattice, fractional coordinates, temperature factors) and reliability factors at the indicated temperatures for RFe_2O_4 (R = Yb, Tm, Lu). The space group is $R\bar{3}m$ in the hexagonal setting, and the Wyckoff positions are indicated for each atom.

	$YbFe_2O_4$			$TmFe_2O_4$			$LuFe_2O_4$
T (K)	400	300	80	400	300	80	400
a (Å)	3.4607(1)	3.4575(1)	3.4495(1)	3.4787(1)	3.4752(1)	3.4657(1)	3.4433(1)
c (Å)	25.1126(1)	25.1098(1)	25.1251(1)	25.0216(1)	25.0169(1)	25.0499(1)	25.2420(1)
Vol. (Å^3)	260.462(1)	259.961(1)	258.912(1)	262.230(2)	261.638(2)	262.230(2)	259.188(1)
R (3*a*):							
B (Å^2)	1.56(2)	1.05(2)	0.87(2)	1.58(3)	1.19(2)	0.96(2)	1.28(1)
Fe (6*c*):							
Z	0.2148(1)	0.2149(1)	0.2150(1)	0.2149(1)	0.2148(1)	0.2147(1)	0.215 24
B (Å^2)	1.15(3)	0.78(3)	0.43(2)	1.24(4)	0.99(3)	0.71(3)	1.04(2)
O1 (6*c*):							
Z	0.1276(2)	0.1291(2)	0.1284(2)	0.1273(2)	0.1274(2)	0.1272(1)	0.1287(2)
B (Å^2)	2.3(2)	1.7(1)	1.4(1)	2.4(1)	1.8(1)	1.3(1)	1.8(1)
O2 (6*c*):							
Z	0.2957(2)	0.2945(2)	0.2945(2)	0.2957(3)	0.2953(2)	0.2943(1)	0.2947(2)
B (Å^2)	1.8(2)	1.2(1)	0.6(1)	2.1(1)	1.4(1)	1.0(1)	1.3(1)
R_p (%)	10.7	8.8	9.9	10.2	9.8	8.6	8.5
R_{Bragg} (%)	5.6	4.7	4.5	5.5	5.2	4.2	5.8
R_F (%)	5.4	4.4	3.5	5.3	4.8	4.0	5.4

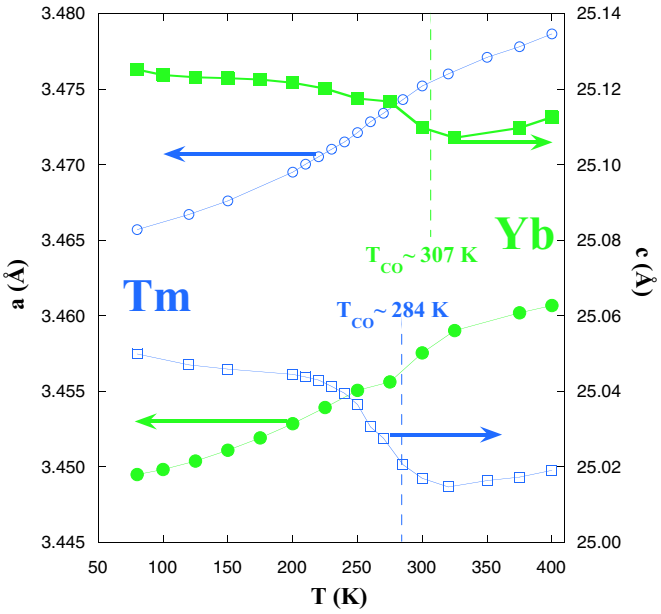

FIG. 3. (Color online) Temperature dependence of lattice parameters for $YbFe_2O_4$ (filled symbols) and $TmFe_2O_4$ (open symbols). Dashed lines indicate the temperature peak in DSC curves [see Fig. 1(a)].

$YbFe_2O_4$, minor changes are observed in the Yb-O distances with a maximum in the temperature dependence around 250 K, close to T_N. Accordingly, the bond length maximum matches a minimum in the BVS value but the calculated valence for Yb^{3+} ranges between 2.99 and 3.04 in the whole temperature range, i.e., very close to the expected value of +3. This suggests a lack of steric strain for this local environment. By looking at the Fe environment in Figs. 4(c) and 4(d), we realize that Fe-O distance in the basal plane (Fe-O_{basal}) decreases with decreasing temperature in both compounds. However, the apical distances follow the opposite trend to that observed in *R*-O bonds. This is because the only degrees of freedom in this structure are the displacements of Fe and O atoms along the *z* direction. Therefore, a lengthening of *R*-O distance involves a shortening in the Fe-O_{apical} bonds. The calculated BVS values for Fe exhibit the reverse behavior to that observed in the *R* atoms, as can be seen later in Fig. 9(c). In this way, Fe valence shows a steplike increase with decreasing temperature for the Tm-based sample and smaller changes for the Yb one. In the former case, the calculated valence above T_{CO} is around 2.29, substantially smaller than the expected value of 2.5. This fact indicates geometric strain, which is relaxed below T_{CO} with the expansion of the *c* axis when the valence of Fe reaches the value of 2.35. On the other hand, the Fe valence in the Yb-based sample ranges between 2.34 and 2.39 with a local maximum in agreement with the minimum in the Yb valence mentioned above.

Regarding the oxygen atoms, the temperature changes in the calculated BVS values are within the error bars. O1 valence shows lower values than expected ones (~ -1.85), while the opposite happens for O2 valence. The latter is significantly higher in the $TmFe_2O_4$ compound (~ -2.15) with respect to the Yb-based sample (~ -2.04), closer to the nominal value of −2. All of these data indicate that the geometric strain is higher for $TmFe_2O_4$ than for $YbFe_2O_4$ and it may be related to the R^{3+} size. Strained structures are formed when it is geometrically impossible to accommodate the bond distances of a given atomic valence in a configuration defined by a set of constraints. The most obvious mechanisms to relax the strain produced by underbonded Fe (and O1) and overbonded *R* (and O2) in the hexagonal structure of Fig. 2 are to reduce the Fe-O1 distance by decreasing the *a* lattice parameter and to raise the *R*-O2 bond length by increasing the *c* axis. Both changes occur at the transition temperature but it is more noticeable in the *c* axis, the largest one.

C. Crystal structure of $LuFe_2O_4$

High resolution x-ray patterns were collected at 400, 350, 300, 285, 250, 220, 205, 150, 125, 100, and 80 K. At 400 K, the x-ray pattern can be refined using the same hexagonal model (space group $R\bar{3}m$) reported in the previous section so $LuFe_2O_4$ is isostructural to $TmFe_2O_4$ and $YbFe_2O_4$ at high temperature. The refined parameters at 400 K are shown in Table I. Upon cooling, strong changes in the patterns are noticeable, as can be seen in Fig. 5. The comparison between the patterns collected at 400 and 260 K show two significant features: first, the occurrence of superstructure peaks in the low temperature pattern indexed as $(h/3\ k/3\ l/2)$ with respect to the hexagonal cell [see Fig. 5(a)]; second, the splitting of a set of main diffraction peaks, as shown in Fig. 5(b). Further cooling leads to additional splitting of more peaks as can be seen in Fig. 5(c). Therefore we expect two structural phase transitions on cooling for this compound.

Superstructure $(h/3\ k/3\ l/2)$ peaks are already seen in the pattern collected at 300 K, below the value of T_{CO} determined by DSC measurements. All reflections can be indexed in the frame of a monoclinic cell with lattice vector $(1\ -1\ 0)$, $(-3\ -3\ 0)$, and $(-1/3\ 1/3\ -2/3)$ with respect to the high temperature hexagonal cell. The systematic extinction of $(h\ k\ l)$ reflections with $h + k = 2n + 1$ indicates a *C*-centered cell. This outcome is in agreement with the results found in a $LuFe_2O_4$ single crystal at 210 K [15]. We used the ISODISPLACE software [36] to explore the possible monoclinic distortions and limited our search to the space group $C2/m$, in agreement with Ref. [15]. There are two possible monoclinic cells depending on the origin of the subgroup with respect to the parent hexagonal cell as indicated in Table II. Each distorted cell may have different active modes belonging to different irreducible representations (Irreps), as indicated in the same table. There is no reason to exclude any of them; therefore, both have been tested. The monoclinic cell with the origin at (0 0 0) yields reasonable fits but fails to refine the intensity of the superstructure peaks. In this solution, the symmetry center is located at the Lu layer and there are four nonequivalent sites for both Lu and Fe atoms. The monoclinic cell with the origin at $(2\ 2\ -1/2)$ yields the best refinement, including the satellites, and it was chosen as the finest solution. Figure 6 displays the monoclinic crystal cell and the relationship between the parent and distorted structures. In this case, the symmetry center lies in the middle of the Fe bilayers. This choice also agrees with the results of Ref. [15]. Figure 7(a) shows a typical refinement using this model, and Table III summarizes the refined structural parameters. The monoclinic cell has four nonequivalent Fe sites as shown in

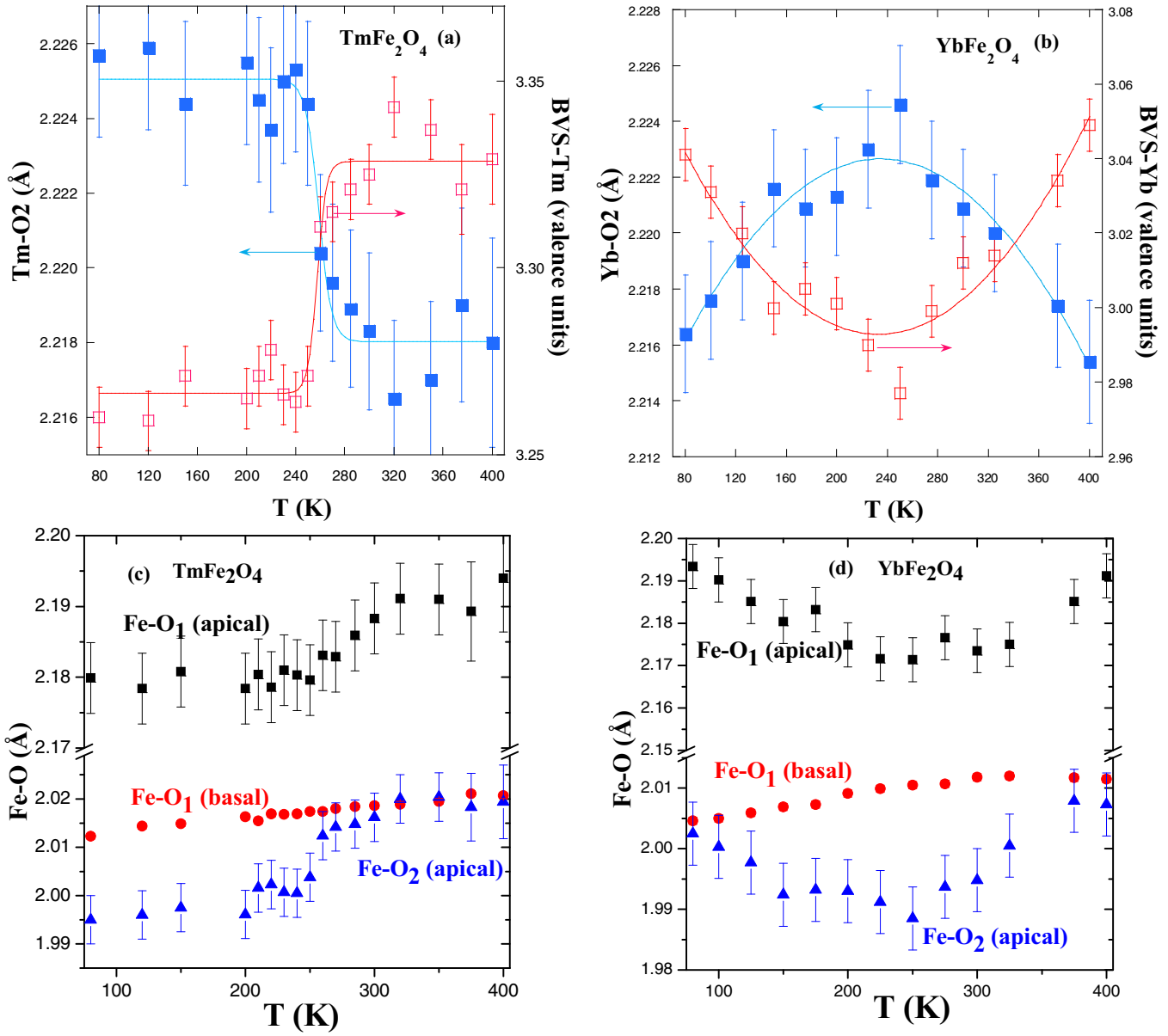

FIG. 4. (Color online) (a) Temperature dependence of R-O2 bond lengths and BVS for $TmFe_2O_4$ (a) and $YbFe_2O_4$ (b). The lines are guides for the eyes. Interatomic distances in the FeO_5 bipyramids for $TmFe_2O_4$ (c) and $YbFe_2O_4$ (d).

Fig. 6. Two of them (Fe1 and Fe4 in Table III and Fig. 6) are located at Wyckoff position $4i$, while the other two (Fe2 and Fe3) are at $8j$. Bond valence sum calculations show different valences for each site: 2.69(3), 2.54(2), 2.29(1), and 2.19(2) for Fe1, Fe2, Fe3, and Fe4, respectively. The maximum charge disproportionation among Fe sites is $0.5e$, and the average charge difference from the mean value of ~2.42 is 0.17(6) valence, i.e., quite below a nominal Fe^{3+}/Fe^{2+} ordering.

Regarding the composition of Fe bilayers along the c axis (see Fig. 6), one bilayer is composed of the pair Fe1-Fe3 (rate 1:2) while the other is formed by the couple Fe2-Fe4 (rate 2:1). According to the BVS values, both bilayers exhibit a similar average Fe valence (~+2.42). This is the main difference between our refinement and Ref. [15], where a difference of +0.1 between Fe bilayers was reported. This small difference may be ascribed either to the study of different specimens or to technical details of the two diffraction techniques but it is noteworthy that a charge difference between bilayers must lead to the occurrence of resonant x-ray scattering (RXS) in $(0\,0\,l/2)_h$ reflections (the h subscript refers to hexagonal cell setting). However, RXS measurements [37,38] have confirmed the lack of resonance for these superstructure reflections in the $\sigma \rightarrow \sigma'$ channel, indicating the lack of a charge modulation along the z direction (and with $l/2$ periodicity) in the Fe sublattice. A pure resonant $(0\,0\,3/2)_h$ reflection was found only in the $\sigma \rightarrow \pi'$ (and $\pi \rightarrow \sigma'$) channel at the Fe L_3 edge, which is ascribed to the magnetic ordering of Fe moments involving $3d$ electrons [38]. These results indicate that our refinement is more reliable to describe the monoclinic cell of $LuFe_2O_4$. Moreover, the lack of RXS intensity at $(0\,0\,l/2)_h$ reflections ($\sigma \rightarrow \sigma'$ or $\pi \rightarrow \pi'$ channels) also negates the approximation to the bimodallike distribution.

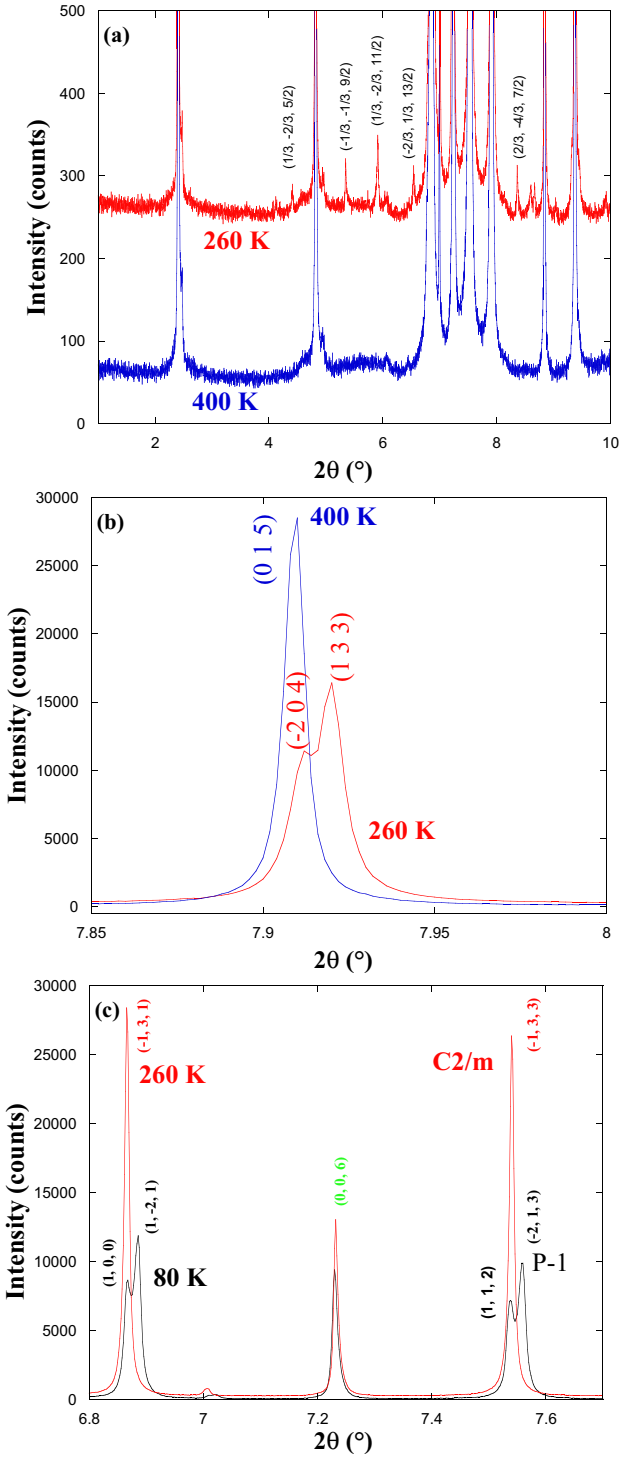

FIG. 5. (Color online) Selected regions of $LuFe_2O_4$ x-ray patterns. Comparison of patterns collected at 400 and 260 K showing (a) the occurrence of superstructure peaks and (b) the splitting of main peaks. (c) Comparison of patterns taken at 260 and 80 K showing additional splitting of peaks at lower temperatures.

Upon decreasing temperature, more peaks are split. In addition, the broadening of $(0\,0\,l)$ reflections at high diffraction angles indicate that the cell is no longer monoclinic but triclinic. These changes are already noticeable in the pattern collected at 150 K, just below the magnetostructural transition at 175 K reported previously [16]. The patterns can be refined using a triclinic cell with lattice vectors (1/2 1/2 0), (−1/2 1/2 0) and (0 0 1) respect to the monoclinic cell. Therefore, it is a primitive cell with a half volume of the C-centered cell, as can also be seen in Fig. 6. ISODISPLACE [36] and AMPLIMODES [25] were used to explore the active modes in the $C2/m \rightarrow P\bar{1}$ transition. There are two kinds of active modes belonging to the Irreps Γ_1^+ and Γ_2^+, the latter being the primary mode to yield the triclinic distortion. First, we have only refined the lattice parameters and the modes belonging to the Irrep Γ_1^+. This procedure is equivalent to refining the triclinic cell with the constraints of $C2/m$ symmetry (i.e., only atomic shifts allowed by the monoclinic symmetry). Surprisingly, the refinement was good, indicating that atomic displacements responsible for the triclinic cell are very tiny. Second, we refined the Γ_2^+ modes. Here, the fit improvement was very small and convergence was poor, with different results depending on the order in which the modes are introduced in the refinement. This fact suggests the presence of several local minima in the fitting procedure. In order to get the most reliable model for the triclinic cell, we have taken into account the results obtained in RXS experiments [37]. These measurements showed the occurrence of resonant scattering in some $(h/3\ k/3\ l)_h$ reflections at low temperature. The existence of these reflections implies a small charge disproportionation of the Fe occupying the Wyckoff positions $(8j)$ in the monoclinic cell (see Fig. 6) [37]. We have explored the role of Γ_2^+ modes in the charge disproportionation of the aforementioned Fe atoms, and we have identified a set of modes acting on Fe and O atoms that lead to expected changes. Each $(8j)$ site in the monoclinic cell splits in two nonequivalent $(2i)$ sites in the triclinic cell. For instance, the Fe3 is split in $Fe3_1$ and $Fe3_2$ (see Table III and Fig. 6). The modes imply atomic displacements in the ab plane, $(-\delta_x, \delta_x, 0)$ and $(\delta_x, -\delta_x, 0)$ for each pair of related atoms ($Fe3_1$ and $Fe3_2$, for instance). The amplitude of refined modes acting on Fe atoms tends to zero while they reach values of ∼0.2 Å for some oxygen atoms. Therefore, the atomic shift of

TABLE II. Lattice vectors and origin of the subgroups $C2/m$ with respect to the parent group $R\bar{3}m$. Directions of the Irreps with active modes for the two types of $R\bar{3}m \rightarrow C2/m$ transitions. The K vector is given for each Irrep, and the broken line means no active modes.

Space subgroup	12 $C2/m$	12 $C2/m$
Lattice vectors	$(-1, 1, 0)$	$(-1, 1, 0)$
	$(-3, -3, 0)$	$(-3, -3, 0)$
	$(1/3, -1/3, 2/3)$	$(1/3, -1/3, 2/3)$
Origin	$(0, 0, 0)$	$(2,2, -1/2)$
Irreps: Γ_1^+ $(0, 0, 0)$ direction	(a)	(a)
Γ_3^+ $(0, 0, 0)$ direction	$(a, -\sqrt{3}a)$	$(a, -\sqrt{3}a)$
$\Sigma_1^+(1/3, -2/3, 0)$ direction	$(0, a, 0, 0, 0, 0)$	$(0, a, 0, 0, \sqrt{3}a, 0)$
$T_1^+(0, 0, 3/2)$ direction	(a)	–
$T_3^+(0, 0, 3/2)$ direction	$(a, 0)$	–
$T_2^-(0, 0, 3/2)$ direction	–	(a)
$T_3^-(0, 0, 3/2)$ direction	–	$(0, a)$
$Y_1(1/3, 1/3, 3/2)$ direction	$(a, 0, 0, 0, 0, 0)$	–
$Y_2(1/3, 1/3, 3/2)$ direction	–	$(a, 0, 0, -\frac{\sqrt{3}}{3}a, 0, 0)$

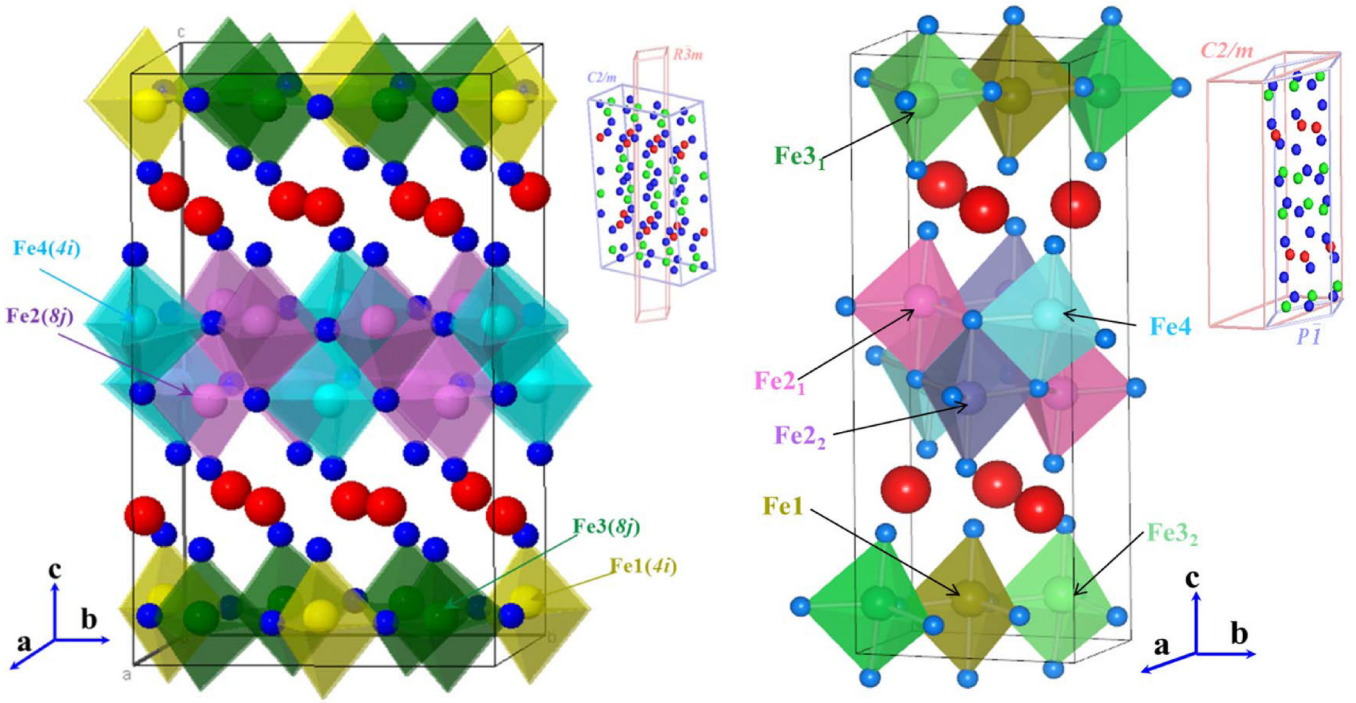

FIG. 6. (Color online) Crystal structure of monoclinic (left) and triclinic (right) structures for $LuFe_2O_4$. The Fe positions within bipyramids are indicated by arrows, while big (red) and small (blue) balls stands for Lu and O atoms, respectively. Insets: (left) Relationship between the parent rhombohedral cell (hexagonal setting) and the monoclinic distorted cell; (right) relationship between the parent C-centered monoclinic cell and the primitive triclinic cell.

the latter atoms seems to differentiate the pairs of $Fe2_1$-$Fe2_2$ and $Fe3_1$-$Fe3_2$ atoms with respect to the monoclinic cell (see Fig. 6). Figure 7(b) shows the refinement at 80 K using this triclinic model, and Table IV shows the refined coordinates.

The temperature dependence of the lattice parameters is shown in Fig. 8. The $R\bar{3}m \rightarrow C2/m$ transition at $T_{CO} \sim 320$ K implies a strong c axis expansion. This feature resembles similar transitions in $TmFe_2O_4$ and $YbFe_2O_4$ compounds. The second transition $C2/m \rightarrow P\bar{1}$ is accompanied by a contraction in the ab plane, and it is only noticeable in $LuFe_2O_4$ sample. In order to verify it, we measured x-ray patterns in a second $LuFe_2O_4$ specimen, which was heated at a rate of 2 K/min from 80 K up to room temperature. We collected more experimental points but the patterns are not appropriate for structural refinement. The ab plane contraction is clearly seen in both measurements. In order to gain insights into the physical significance of the transitions, BVS was calculated for all atoms. Lu^{3+} cations are overbonded in the rhombohedral cell as BVS value is higher than the ideal oxidation state of 3+, as shown in Fig. 9(a). In the $R\bar{3}m \rightarrow C2/m$ transition, the average Lu valence approaches its ideal value with a significant decrease. In the $C2/m \rightarrow P\bar{1}$ transition, the Lu1 valence undergoes an additional small decrease, while the valence of Lu2 atoms remains almost unchanged. The Fe sublattice suffers more drastic changes in both transitions, as can be seen in Fig. 9(b). Fe is a bit underbonded in the rhombohedral cell of $LuFe_2O_4$ and the average valence slightly increases at the $R\bar{3}m \rightarrow C2/m$ transition. There are four different Fe sites in the $C2/m$ cell with four different valence states. They range between ~2.2 and ~2.70. In this model, the Fe bilayers composed of Fe1+Fe3 and Fe2+Fe4 show the same average valence value for Fe atoms, quite close to the ideal value of +2.5. At the $C2/m \rightarrow P\bar{1}$ transition, Fe2 and Fe3 are split in two different oxidation states with a difference of around $0.2e$, while Fe1 remains without significant changes and Fe4 shows a small valence increase. The result at 80 K can be viewed as a trimodal charge distribution by pairing Fe4-$Fe3_1$ (average valence +2.27 at 80 K), $Fe3_2$-$Fe2_2$ (+2.46 at 80 K), and Fe1-$Fe2_1$ (+2.70). The resulting charge distribution remains with the two Fe bilayers with a similar average Fe charge [37]. Underbonded Fe atoms are a common feature in the rhombohedral cell of RFe_2O_4 samples, as can be seen in Fig. 9(c) where the temperature dependence of BVS values of the three ferrites is compared. As R^{3+} size diminishes, the strains in the Fe-O sublattice also decrease, and Fe valence is closer to the nominal value for the Lu-based compound. In the same way, the strain is relaxed with decreasing temperature in the three samples, but this relaxation is more effective in $LuFe_2O_4$ with the two structural phase transitions.

IV. CONCLUSIONS

The detailed study of the crystal structure of RFe_2O_4 (R = Tm, Yb, and Lu) ferrites has revealed several facts. These compounds exhibit a mixed valence state of the Fe atoms at high temperatures. The crystal structure is rhombohedral but it is quite strained. This structural strain is evident for two reasons. First, the refined temperature factors are very high, especially for oxygen atoms, indicating a strong disorder. This agrees with the dynamic disorder deduced around the Fe atoms in a previous x-ray absorption investigation of these ferrites [32]. Second, the BVS analysis shows that R atoms

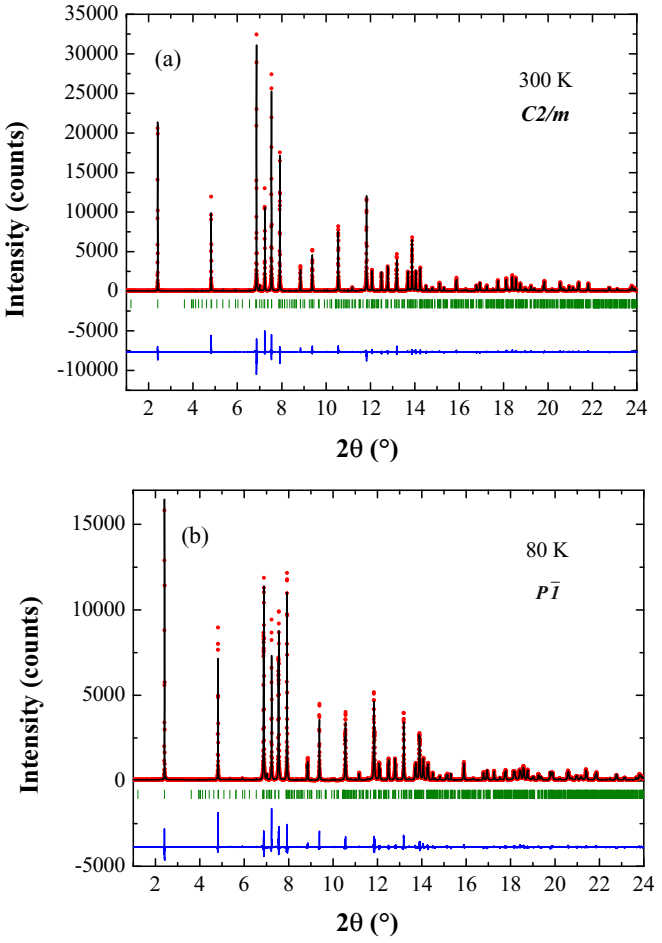

FIG. 7. (Color online) Rietveld refinement of $LuFe_2O_4$ at (a) 300 and (b) 80 K. Points and continuous line refer to experimental and calculated patterns, respectively. The difference is plotted at the bottom with the allowed reflections.

are overbonded, whereas Fe atoms are underbonded, and the deviation from the valence sum rule increases with increasing the R size. This explains the lack of RFe$_2$O$_4$ phase in the phase diagram of Fe-Fe$_2$O$_3$-R$_2$O$_3$ systems with R^{3+} bigger than Ho^{3+} [39].

The strain relaxation on cooling occurs in different ways depending on the R atom. For R = Yb and Tm, cooperative shifts of the atoms along the z direction lead to a sudden expansion of the c axis at T_{CO}. This expansion is coupled to a small contraction of the ab plane and a turning point in the electrical resistance. The resulting structure is still strained but remains rhombohedral until 80 K. The occurrence of an incommensurate charge density wave [20] might be not detected by the sensitivity of x-ray powder diffraction measurements but cannot be discarded for both samples.

A different behavior is observed in $LuFe_2O_4$ where distortions are fully ordered at low temperatures. A similar expansion of the c axis is observed at T_{CO}, but it is coupled to a structural transition from $R\bar{3}m$ to $C2/m$ symmetry. This transition can be viewed as the result of condensing modes that belong to the Irrep Y_2. The resulting structure shows the Lu atoms in an appropriate environment according to BVS, and

TABLE III. Wyckoff positions, fractional coordinates, and temperature factors of $LuFe_2O_4$ at 300 K ($C2/m$ space group). Coordinates arise from the refinement of amplitude modes so some values without errors imply negligible mode amplitude. The refined lattice parameters are a = 5.958 83(1) Å, b = 10.315 46(2) Å, c = 16.956 37(3) Å, and β = 96.795°(1) with the following reliability factors (%): R_p = 7.2, R_{Bragg} = 4.82, and R_F = 4.74. Numbers in parentheses indicate standard deviations of the last significant digits.

Atom	Site	x	y	z	B (Å^2)
Lu1	4i	0.2500(3)	½	0.2434(1)	0.92(1)
Lu2	8j	0.2500(1)	0.3333	0.7467(1)	0.92(1)
Fe1	4i	0.1453(7)	½	0.9272(1)	0.78(2)
Fe2	8j	0.1431(4)	0.3333	0.4272(1)	0.78(2)
Fe3	8j	0.3613(4)	0.3333	0.0728(1)	0.78(2)
Fe4	4i	0.3636(7)	½	0.5728(1)	0.78(2)
O1	4i	0.291(2)	½	0.4478(6)	1.23(7)
O2	4i	0.162(2)	½	0.0605(6)	1.23(7)
O3	8j	0.3027(11)	0.3333	0.9458(4)	1.23(7)
O4	8j	0.3027(11)	0.3333	0.5584(4)	1.23(7)
O5	4i	0.399(3)	½	0.6908(2)	1.23(7)
O6	4i	0.116(3)	½	0.8092(2)	1.23(7)
O7	8j	0.395(2)	0.326(1)	0.1908(2)	1.23(7)
O8	8j	0.112(2)	0.341(1)	0.3092(2)	1.23(7)

the Fe atoms are split into four nonequivalent sites with four different nominal valences.

$LuFe_2O_4$ undergoes a further transition on cooling. The strong splitting of some diffraction peaks can be accounted for by a primitive triclinic cell with half volume of the monoclinic one. Two Fe of the monoclinic cell are split, resulting in a total of six nonequivalent Fe sites. This splitting is accompanied by a nearly symmetric charge disproportionation, and the resulting Fe valences can be grouped in a trimodal distribution. The aver-

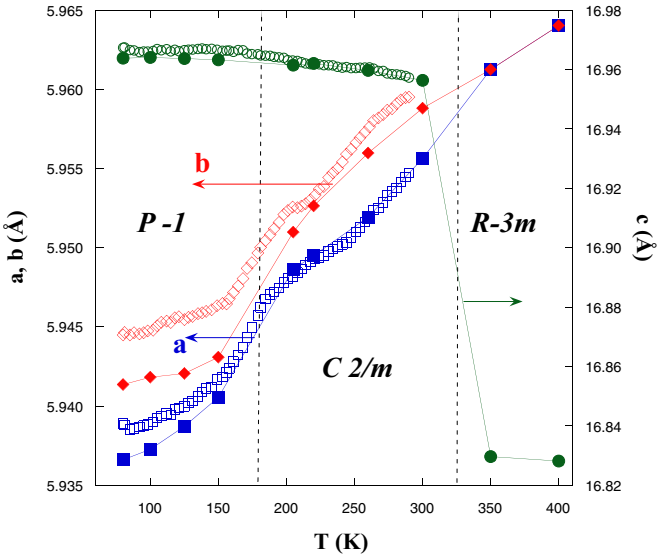

FIG. 8. (Color online) Temperature dependence of the lattice parameters in the monoclinic setting of two $LuFe_2O_4$ specimens. Filled symbols correspond to the first specimen with high resolution measurements performed at selected temperatures. Open symbols correspond to the second specimen with data acquired (every 5 min) in a heating ramp of 0.5 K min^{-1}.

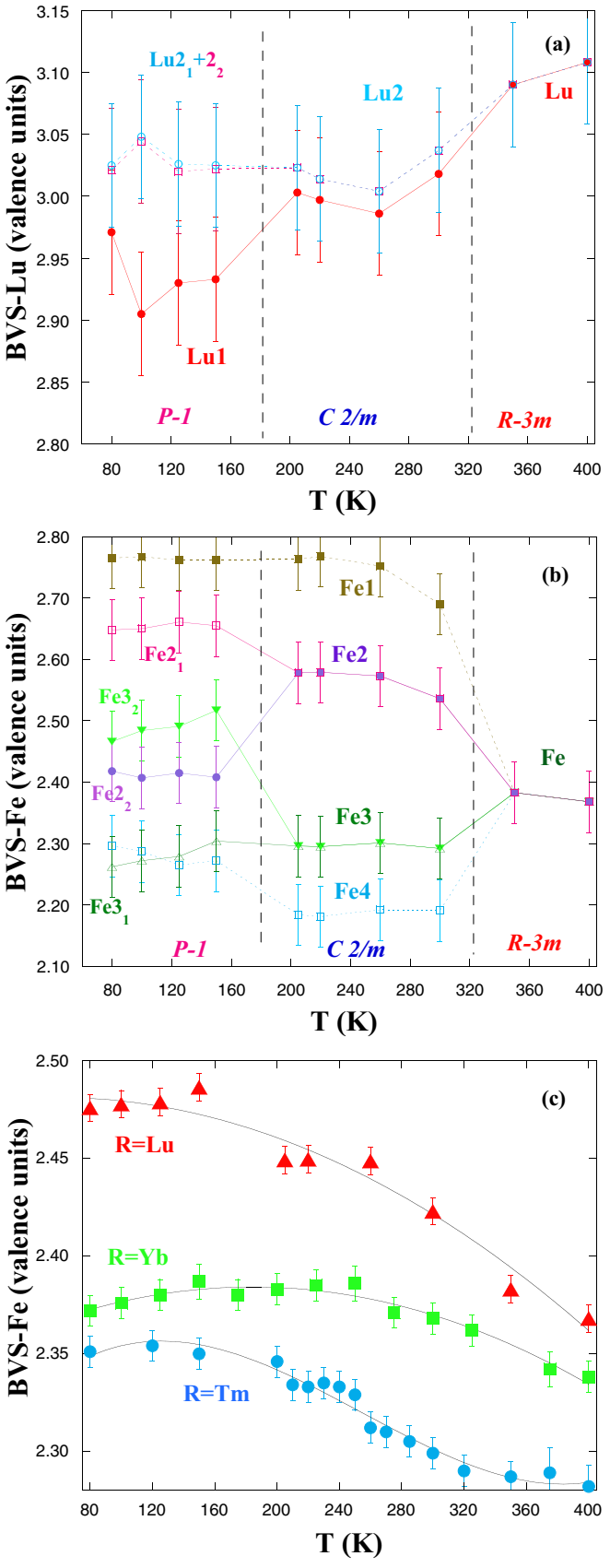

FIG. 9. (Color online) Temperature dependence of BVS for (a) Lu and (b) Fe atoms in $LuFe_2O_4$. (c) Temperature dependence of BVS for Fe in the three RFe_2O_4 compounds. The data for Lu-based sample below T_{CO} correspond to the average values.

TABLE IV. Wyckoff positions, refined fractional coordinates and temperature factors of $LuFe_2O_4$ at 80 K (P-1 space group). The refined lattice parameters are $a = 5.9369(1)$ Å, $b = 5.9415(1)$ Å, $c = 16.9600(1)$ Å, $\alpha = 93.352(1)$, $\beta = 93.298(1)$, and $\gamma = 119.847(1)$ with the following reliability factors (%): $R_p = 8.16$, $R_{Bragg} = 4.26$, and $R_F = 3.19$.

Atom	Site	x	y	Z	B (Å^2)
Lu1	2i	0.7499(12)	0.7499(12)	0.2418(2)	0.63(1)
Lu2$_1$	2i	0.9161(13)	0.5843(13)	0.7472(2)	0.63(1)
Lu2$_2$	2i	0.4157(13)	0.0839(13)	0.2528(2)	0.63(1)
Fe1	2i	0.6452(12)	0.6453(12)	0.9272(2)	0.35(2)
Fe2$_1$	2i	0.5237(17)	0.1880(17)	0.5730(2)	0.35(2)
Fe2$_2$	2i	0.8121(17)	0.4762(17)	0.4270(2)	0.35(2)
Fe3$_1$	2i	0.3128(17)	0.9745(17)	0.9282(2)	0.35(2)
Fe3$_2$	2i	0.0254(17)	0.6873(17)	0.0718(2)	0.35(2)
Fe4	2i	0.8636(12)	0.8636(12)	0.5728(2)	0.35(2)
O1	2i	0.799(5)	0.799(5)	0.4487(2)	0.80(6)
O2	2i	0.660(5)	0.660(5)	0.0611(19)	0.80(6)
O3$_1$	2i	0.977(5)	0.632(5)	0.9463(16)	0.80(6)
O3$_2$	2i	0.354(5)	0.038(5)	0.0537(16)	0.80(6)
O4$_1$	2i	0.828(4)	0.516(4)	0.5582(14)	0.80(6)
O4$_2$	2i	0.504(4)	0.151(4)	0.4418(14)	0.80(6)
O5	2i	0.901(5)	0.901(5)	0.6903(3)	0.80(6)
O6	2i	0.622(5)	0.622(5)	0.8090(2)	0.80(6)
O7$_1$	2i	0.070(4)	0.723(4)	0.1887(6)	0.80(6)
O7$_2$	2i	0.277(4)	0.930(4)	0.8113(6)	0.80(6)
O8$_1$	2i	0.772(4)	0.455(4)	0.3095(6)	0.80(6)
O8$_2$	2i	0.545(4)	0.227(4)	0.6904(6)	0.80(6)

age charge in the two Fe bilayers remains around +2.45 in both (monoclinic and triclinic) structures. This implies that there is no charge difference between neighboring Fe bilayers along the c axis as previously reported [15], and this result is entirely consistent with recent RXS experiments on $LuFe_2O_4$ [37,38].

The maximum charge disproportionation found in $LuFe_2O_4$ below T_{CO} is half of that expected in the formation of Fe^{2+}/Fe^{3+} ions, so a full CO transition is unlikely to account for the properties of this transition. Therefore, the term of CO may not be appropriate to describe the structural transition developed by the three compounds at T_{CO}. Minor and similar changes are observed in the electrical properties of the studied samples, and this is true even for $YbFe_2O_4$ and $TmFe_2O_4$ without noticeable charge disproportionation below T_{CO}. It is more likely that the small increase in the band gap at T_{CO} is due to the condensation of a soft mode.

ACKNOWLEDGMENTS

Financial support from the Spanish Ministerio de Economía y Competitividad (Project No. MAT2012-38213-C02-01), and Diputación General de Aragón (DGA) to Caracterización de Materiales con Radiacción de Sincrotrón (CAMRADS) group is acknowledged. S. Lafuerza thanks DGA for the research grant. The authors would like to acknowledge the use of servicios de apoyo a la investigación from Universidad de Zaragoza. We also thank ESRF for beam time allocation and special thanks to Andy Fitch for the technical assistance.

[1] A. P. Pyatakov and A. K. Zvezdin, Physic-Uspekhi **55**, 557 (2012).
[2] D. I. Khomskii, J. Magn. Magn. Mat. **306**, 1 (2006).
[3] K. F. Wang, J.-M. Liu, and Z. F. Ren, Adv. Phys. **58**, 321 (2009).
[4] N. Ikeda, H. Ohsumi, K. Ohwada, K. Ishii, T. Inami, K. Kakurai, Y. Murakami, K. Yoshii, S. Mori, Y. Horibe, and H. Kitô, Nature **436**, 1136 (2005).
[5] J. van der Brink and D. I. Khomskii, J. Phys.: Condens. Matter **20**, 434217 (2008).
[6] K.-T. Ko, H.-J. Noh, J.-Y. Kim, B.-G. Park, J.-H. Park, A. Tanaka, S. B. Kim, C. L. Zhangand, and S.-W. Cheong, Phys. Rev. Lett. **103**, 207202 (2009).
[7] N. Ikeda, K. Kohn, N. Myouga, E. Takahashi, H. Kitôh, and S. Takekawa, J. Phys. Soc. Jpn. **69**, 1526 (2000).
[8] M. A. Subramanian, T. He, J. Chen, N. S. Rogado, T. G. Calvarese, and A. W. Sleight, Adv. Mater. **18**, 1737 (2006).
[9] T. Kambe, Y. Fukada, J. Kano, T. Nagata, H. Okazaki, T. Yokoya, S. Wakimoto, K. Kakurai, and N. Ikeda, Phys. Rev. Lett. **110**, 117602 (2013).
[10] C. H. Li, F. Wang, Y. Liu, X. Q. Zhang, Z. H. Cheng, and Y. Sun, Phys. Rev. B **79**, 172412 (2009).
[11] P. Ren, Z. Wang, W. G. Zhu, H. A. Huan, and L. Wang, J. Appl. Phys. **109**, 074109 (2011).
[12] D. Niermann, F. Waschkowski, J. de Groot, M. Angst, and J. Hemberger, Phys. Rev. Lett. **109**, 016405 (2012).
[13] A. Ruff, S. Krohns, F. Schrettle, V. Tsurkan, P. Lunkenheimer, and A. Lloid, Eur. Phys. J. B **85**, 290 (2012).
[14] S. Lafuerza, J. García, G. Subías, J. Blasco, K. Conder, and E. Pomjakushina, Phys. Rev. B **88**, 085130 (2013).
[15] J. de Groot, T. Mueller, R. A. Rosenberg, D. J. Keavney, Z. Islam, J.-W. Kim, and M. Angst, Phys. Rev. Lett. **108**. 187601 (2012).
[16] A. D. Christianson, M. D. Lumsden, M. Angst, Z. Yamani, W. Tian, R. Jin, E. A. Payzant, and S. E. Nagler, Phys. Rev. Lett. **100**, 107601 (2008).
[17] M. Tanaka, K. Siratori, and N. Kimizuka, J. Phys. Soc. Jpn. **53**, 760 (1984).
[18] M. Kishi, S. Miura, Y. Nakagawa, N. Kimizuka, I. Shindo, and K. Siratori, J. Phys. Soc. Jpn. **51**, 2801 (1982).
[19] K. Yoshii, N. Ikeda, and A. Nakamura, Physica B **378**, 585 (2006).
[20] A. J. Hearmon, D. Prabhakaran, H. Nowell, F. Fabrizi, M. J. Gutmann, and P. G. Radaelli, Phys. Rev. B **85**, 014115 (2012).
[21] X. S. Xu, J. de Groot, Q. C. Sun, B. C. Sales, D. Mandrus, M. Angst, A. P. Litvinchuk, and J. L. Musfeldt, Phys. Rev. B **82**, 014304 (2010).
[22] A. N. Fitch, J. Res. Natl. Inst. Stand. Technol. **109**, 133 (2004).
[23] J. Rodríguez-Carvajal, Physica B **192**, 55 (1993) http://www.ill.eu/sites/fullprof/.
[24] D. Orobengoa, C. Capillas, M. I. Aroyo, and J. M. Pérez-Mato, J. Appl. Crystallogr. **42**, 820 (2009).
[25] J. M. Pérez-Mato, D. Orobengoa, and M. I. Aroyo, Acta Crystallogr. A **66**, 558 (2010).
[26] J. Blasco, S. Lafuerza, J. García, G. Subías, M. C. Sánchez, V. Cuartero, and J. Stankiewicz, Dalton Trans. **40**, 3211 (2011).
[27] J. García and G. Subías, J. Phys:Condens. Matter **16**, R145 (2004).
[28] M. Tanaka, J. Akimitsu, Y. Inada, N. Kimizuka, I. Shindo, and K. Siratori, Sol. State. Comm. **44**, 687 (1982).
[29] Y. Sun, J. Z. Cong, Y. S. Chai, L. Q. Yan, Y. L. Zhao, S. G. Wang, W. Ning, and Y. H. Zhang, Appl. Phys. Lett. **102**, 172406 (2013).
[30] F. Wang, J. Kin, and Y.-J. Kim, Phys. Rev. B **80**, 024419 (2009).
[31] M. H. Phan, N. A. Frey, H. Srikanth, M. Angst, B. C. Sales, and D. Mandrus, J. Appl. Phys **105**, 07E308 (2009).
[32] S. Lafuerza, J. García, G. Subías, J. Blasco, and V. Cuartero, Phys. Rev. B **89**, 045129 (2014).
[33] R. D. Shannon, Acta Cryst. A **32**, 751 (1976).
[34] I. D. Brown, Acta Cryst. B **48**, 553 (1992).
[35] N. E. Brese and M. O'Keeffe, Acta Cryst. B **47**, 192 (1991).
[36] B. J. Campbell, H. T. Stokes, D. E. Tanner, and D. M. Hatch, J. Appl. Cryst. **39**, 607 (2006).
[37] S. Lafuerza, G. Subías, J. García, J. Blasco, G. Nisbett, K. Conder, and E. Pomjakushina, Phys. Rev. B **90**, 085130 (2014).
[38] J. de Groot, K. Marty, M. D. Lumsden, A. D. Christianson, S. E. Nagler, S. Adiga, W. J. H. Borghols, K. Schmalzl, Z. Yamani, S. R. Bland, R. de Souza, U. Staub, W. Schweika, Y. Su, and M. Angst, Phys Rev. Lett. **108**, 037206 (2012).
[39] N. Kimizuka, E. Muromachi, and K. Siratori, in *Handbook on the Physics and Chemistry of Rare Earths*, edited by K. A. Gschneidner, Jr. and L. Eyring (Elsevier Sci. Press, North-Holland, 1990), Vol. 23, p. 283.